Experimental investigation on the spalling failure of a railway turnout made from Hadfield steel

LUO, Quanshun <http://orcid.org/0000-0003-4102-2129>, KITCHEN, Matthew, LI, Jianbin, LI, Wenbo and LI, Yanzheng

Wear 523 (2023) 204779

Contents lists available at ScienceDirect

Wear

journal homepage: www.elsevier.com/locate/wear

Experimental investigation on the spalling failure of a railway turnout made from Hadfield steel

Quanshun Luo [a,*], Matthew Kitchen [a], Jianbin Li [b], Wenbo Li [c], Yanzheng Li [b]

[a] Materials and Engineering Research Institute, Sheffield Hallam University, Sheffield, UK
[b] China Railway High-Tech Industry Corporation Limited, Beijing, China
[c] China Railway Baoji Bridge Group Co., Ltd, Baoji, Shaanxi Province, China

ARTICLE INFO

Keywords:
Turnout failures
Austenitic Hadfield steel
Strain hardening and embrittlement
Strain induced martensite
Mechanical twins

ABSTRACT

In a rail track structure, a turnout is used as a transition between straight and branching rails and therefore withstands complex dynamic rolling and impact loading. This paper reports a comprehensive failure investigation of a railway off-track turnout made from Hadfield austenitic cast steel. The worn turnout was examined using optical microscopy, scanning electron microscopy, micro-hardness, and quantitative X-ray diffraction analyses. A ball-on-disc sliding wear test was also applied to evaluate the impact of work-hardening on the wear property. The turnout exhibited surface embrittlement, severe cracking, delamination, and spalling characteristics. Severe plastic deformation of the worn turnout was observed with the formation of densely packed mechanical twins, which facilitated crack propagation. The rail top developed a gradient hardness ($HV_{0.1}$) profile from the rail top of 8.9 GPa, the cracked subsurface of 5.9 GPa to the bulk steel of 2 GPa. The rail top was also found to have accumulated an extremely high residual compressive stress of 500–650 MPa. Strain induced martensite transformation was repeatedly evidenced by X-ray diffraction peak of the ferritic (110) plane although the highly strained and nanocrystallised ferrite was only detected on the severely deformed rail top. Comparative sliding wear tests showed highly deteriorated wear resistance of the strain-hardened rail top as compared to the bulk steel.

1. Introduction

Railway systems have been a major ground transportation of passengers and cargos for more than a century. In recent years, high performance rail materials are highly demanded due to the increase in cargo loads and vehicle speed, which is especially true for turnouts and crossings [1]. In a rail track structure, a turnout is used as a transition between straight and branching rails and therefore withstands complex dynamic rolling and impact loading. In particular, the discontinuity in a pairing wing rail and turnout causes repeated heavy impact loads, which can be several times higher than the normal rolling loads from vehicle wheels [2–4].

A high-carbon and high-manganese austenitic steel, known as the Hadfield steel since its invention in 1880's, has been the major material used to produce railway turnouts to date, although some alternative steels of better wear resistance were introduced in the last 30 years. Moreover, Hadfield steels are still widely used to manufacture wear resistant parts in many industries such as impact hammers, crusher jaws and cones, grinding mill liners, bucket teeth of excavators, crawler treads of tractors, and railway turnouts [5–7]. These applications are attributed to the excellent strain hardening capability and good toughness of Hadfield steel, along with the ability to produce various sizes of castings at relatively low cost. However, Hadfield steels have low hardness, low strength and inferior strain hardening at non-severe loading conditions. These have led to the development of alterative steels, such as austenitic medium manganese steel [8,9] and Fe-Mn-Al-C austenitic steel [10,11], with better wear resistance and higher strength.

The strain hardening mechanisms of Hadfield steel have been studied since its invention. There have been several conclusive strain hardening mechanisms reported [12]. Hadfield steels have high carbon and manganese content which helps stabilise the austenite phase by reducing the martensite transformation temperature (Ms) to −197 °C, lower the stacking fault energy to facilitate the formation of extended dislocations, and promote the formation of Mn-C atomic clusters [6,13]. The strain hardening mechanisms of Hadfield steels were reviewed to include slipping-induced dislocation multiplication, dislocation glide involving

* Corresponding author. Materials and Engineering Research Institute, Sheffield Hallam University, Sheffield, South Yorkshire, S1 1WB, United Kingdom.
E-mail address: q.luo@shu.ac.uk (Q. Luo).

https://doi.org/10.1016/j.wear.2023.204779
Received 13 September 2022; Received in revised form 13 December 2022; Accepted 11 January 2023
Available online 28 March 2023

interactions with carbon-manganese atomic clusters, mechanical twinning along more than one crystalline orientations, and dynamic strain aging involving the peening effect of solute atoms to dislocations [5–7,12–20]. In addition, strain induced martensite transformation was also claimed as a hardening mechanism whereas it was not experimentally approved in high-carbon and high-manganese Hadfield steel. Comparing to Hadfield steel, medium manganese steels were reported to show strain induced martensite transformation in non-severe loading conditions [8,9]. Meanwhile, austenitic manganese steels with higher Mn and aluminium contents, such as Fe-33.6Mn-8.8Al-1.38C [11], Fe-25.1Mn-6.6Al-1.3C [21] and Fe-23.38Mn-6.86Al-1.43C [10], were developed to significantly improve of their strength properties, which was achieved through the precipitation of κ-$(Fe,Mn)_3AlC$ compound from the austenitic matrix in an aging process, after the austenitic solutioning treatment.

To date, austenitic Hadfield steel is still widely used worldwide to manufacture railway turnouts, where spalling wear is recognised as one of major failures [1–4,6,22]. Fig. 1 shows the photographs of two used turnouts which were taken from off-track crossings. Severe spalling failures are highlighted in the pictures. It has been shown that, the severe loads of railway turnouts include compression arising from rolling contacts, shear loads of various directions, and impact loads due to wheel shifting from wing rail to frog rail [2]. The increased train speed and weight capacity of modern railway systems has further enhanced the loading severity on the rails and turnouts [1,22,23]. Guo observed the strain hardening of a used Hadfield steel turnout of HV600 and HV500 at depths of 1.0 mm and 3.0 mm, respectively [4]. Zhang summarised the failures of austenitic manganese steel turnouts to include accumulative deformation, wear, and spalling, whereas major evidences included mechanical twinning and intergranular cracking observed in subsurface zone of a failure turnout [24]. Enhanced mechanical twinning and strain hardening were also reported in the dry sliding wear of Hadfield steels under varying loads [16].

Up to date, however, the spalling failure mechanisms of Hadfield steel, mainly for the lack of research on the deformation induced embrittlement. Although the strain hardening has been known to be an outstanding property of Hadfield steels, it is not clear how the strain hardening affects the wear resistance. There is also lack of convincible experimental verification about the occurrence of strain induced austenite-to-martensite transformation in addition to other hardening mechanisms [6,7,16–18]. Although the formation of residual compressive stresses in plastically deformed surfaces is known to have a strong impact on fatigue failure, few experimental measurements on rail surfaces were reported only in recent years [22,25].

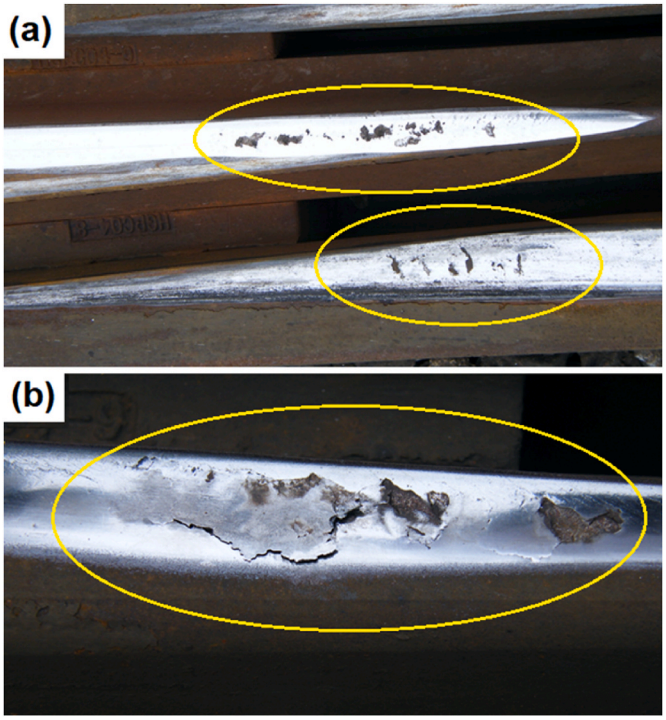

Fig. 1. Spalling failures observed on the load-bearing top of turnouts.

In this paper, we present details of experimental characterisation of a failed turnout of austenitic Hadfield cast steel using optical and electron microscopy, hardness profiling measurements, and quantitative X-ray diffraction (XRD). Evidence of strain induced martensite transformation, as well as high residual compressive stresses, on the rail top surface was obtained from the XRD analyses. Cross-sectional microscopy revealed the high-density mechanical twins which promoted subsurface crack propagation in the extremely strain-hardened zone. Moreover, the strain-hardening induced embrittlement of the rail surface was confirmed to deteriorate its sliding wear resistance.

2. Experimental

The failed Hadfield manganese steel turnout was removed from a straight track, from which the railway frog was removed for failure investigation. Fig. 2 is a photograph of the turnout, which is 270 mm long, with a tapering width from 15 mm to 45 mm in the narrow and broad ends, respectively. A ridge line was observed on the top surface with both sides, marked as A and B in Fig. 2, showing evidence of spalling marks along the length. However side A had a greater concentration of spalling pits and was therefore the focus of the failure analysis.

Using a SiC-resin abrasive cutting wheel with water-based coolant, samples for the failure analysis were sectioned from three places of the turnout, marked as I, II and III in Fig. 2. The samples were cleaned using acetone and cotton bud to remove most of the oxidation product and dried in air. Two areas of the sample were selected for microstructural characterisation. The first area was created by carefully removing approximately 40 μm from the top surface to produce a metallographic flat area. The second area was made by taking a perpendicular cross-section from the top surface. The samples were then prepared using standard metallographic practices to a 1 μm finish and etched in a 2% nital solution.

Tensile and V-notch Charpy impact specimens were produced from longitudinal bars that were sectioned from the bottom of the turnout. The tensile specimens were machined to a diameter of 15 mm at the ends and 10 mm in the tensile length, respectively. The impact specimens were machined with a square cross section of 10 × 10 mm^2, approximately 55 mm long, and a 2 mm deep V-notch. The tensile and Charpy impact tests were performed in triplicate, to obtain the average values and standard deviation, at room temperature, following the standards BS EN ISO 6892-1-2019 and BS EN ISO 148–1:2016, respectively.

The chemical composition of the steel was analysed using a spark optical emission spectroscope. An optical microscope (OPM) was employed for microstructural characterisation at low magnifications. A field-emission scanning electron microscope (SEM) was employed for several observations, including microstructure characterisation at high spatial resolution, the spalling failure and sliding wear, and fractography after the tensile and impact tests. The observations were made in secondary electron imaging (SEI) mode at the accelerating voltage of 20 kV.

An X-ray diffractometer, using a radiation of Kα-Co (wavelength λ = 0.1789 nm, anode at 40 kV and 40 mA), was employed to perform crystallographic analysis and residual stress measurements. The diffraction curves for crystallographic analyses were acquired using the ***θ-2θ*** scan mode, with a step size of 0.026° and a scan rate of $0.0022^\circ \cdot s^{-1}$. The full-width-at-half-maximum (FWHM) of every diffraction peak was measured to express the peak breadth (β), with an instrumental peak breadth (β_i) of 0.09°, measured using a standard silicon sample. The deformation induced lattice microstrain and grain refinement were

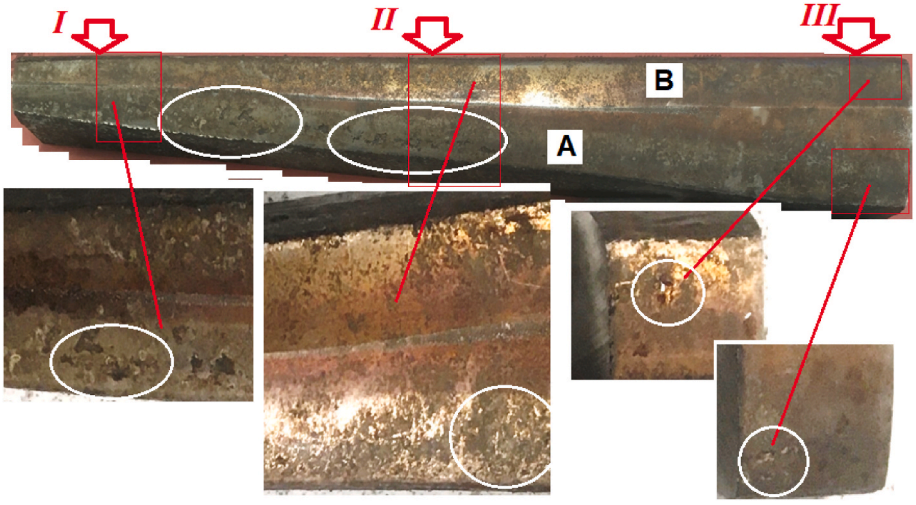

Fig. 2. Hadfield steel samples cut from a used turnout.

estimated using the Wilson ($\varepsilon = \frac{0.25\cdot(\beta-\beta_0)}{tan(\theta)}$) and Scherrer equations ($t = \frac{0.94\cdot\lambda}{(\beta-\beta_i)\cdot cos\ \theta}$), respectively, where t is the size of the crystallite [26–29]. The residual stress of the rail surfaces were measured using two methods, namely, the traditional and modified $sin^2\psi$ methods [30,31]. In the measurement, the (311) peak of austenite was selected to acquire diffraction peaks under the Ω-2θ mode for a series of off-axis angles of ψ = 0°, ±12°, ±21.5°, ±28.5°, ±34.5° and ±40°. For the calculation of the residual stress, it was assumed that the Hadfield steel had an elastic modulus (E) and Poisson's ratio (ν) of 210 GPa and 0.30, respectively [32].

The wear property of the severely deformed rail top was evaluated to compare with the wear property of the bulk steel. Reciprocating sliding wear tests were performed under ambient conditions using a 6 mm diameter WC ball counterpart. The tests were undertaken at the same sliding length of 8 mm and reciprocating frequency of 47 passes per minute. Each test ran for 120 min, which resulted in 5640 sliding passes and a total sliding distance of 45.12 m. The tests were made under three applied normal loads of 49 N, 29.4 N and 9.8 N to represent different loading severities. After each test, three depth profiles were measured across the width of the wear track within the central section along the wear track, from which the cross-section area was calculated to estimate the volume loss V. Accordingly, the wear coefficient k was calculated from the wear volume V, the applied load W, and the total sliding distance L using the equation $k = \frac{V}{W\cdot L}$.

3. Results

3.1. Characterisation of the bulk steel

Table 1 shows the chemical compositions of the turnout, whereas the mechanical properties are listed in Table 2. The analysis confirmed that the turnout was made from high-manganese Hadfield steel without any other alloying elements. The steel exhibits low hardness and yielding strength (i.e., the stress at 0.2% strain), high plasticity and toughness, and good strain hardening capacity. These properties are similar to the mechanical properties of Hadfield steels reported in literature [24,33]. X-ray diffraction analysis indicated single-phase austenitic crystalline structure. Microscopic observations revealed coarse equaxial granular microstructure.

Table 1
The chemical compositions the manganese steel turnout.

C	Si	Mn	P	Cr	Fe
0.98 ± 0.01	0.51 ± 0.01	13.05 ± 0.16	0.02	0.03	Balance

3.2. Characterisations of the rail top surface

Fig. 3 show selected SEM observations of the rail top of the turnout, where visual inspection found severe spalling damage (Side A in Fig. 2). The observed area located on the severe damaged side, i.e., Side A as shown in Fig. 3a, had a rough appearance due to the high concentration of spalling failures, as well as corrosion induced contaminants. A small area, marked as 'b', is shown at an increased magnification in Fig. 3b, where three features were identified, including relatively rough and deep spalling pits as marked 'X' (Fig. 3b and d), broad delamination areas as marked 'D' (Fig. 3b and c), and the remained rail surface as marked 'T' (Fig. 3c). The delaminated surface exhibits a brighter contrast, when compared to the remaining rail surface, owing to the increased roughness. The majority of the imaged area contained spalling and delamination characteristics resulting in the formation of isolated islands of the remaining rail surface. This phenomenon indicates the high severity of the spalling and delamination failure, which is consistent with the spalling failures of Hadfield turnouts reported by other researchers [1,6,22,24].

To further clarify the morphology of the different features, two selected regions, as marked 'c' and 'd', were observed at higher magnifications (Fig. 3c and d, respectively). In Fig. 3c, the remained rail surface (marked 'T') is relatively smooth and featureless, whereas the delamination area is covered with very fine needle-like substance which were determined to contain high intensity of oxygen, suggestive of free-grown corrosion products. These contaminants modified the original morphology of the delamination by masking the original features. However, the cycled area between the two delamination zones shows fine fragments having straight edges, which confirm that the delamination followed a brittle cracking mechanism. Similar brittle failures were observed frequently in other areas. Fig. 3d is a high-magnification image observing the bottom of two spalling pits (marked 'X'). The spalling detachment had left brittle fracture features as well as secondary cracking. These features suggest that the spalling occurred at certain depths beneath the load-bearing top.

In order to characterise the top layer, where the delamination and spalling took place, a 5-mm wide flat band was created by metallographic grinding and polishing, which was then etched using 2% nital to reveal the microstructure, approximately 20–40 μm, beneath the top surface. Fig. 4 shows the results of SEM observations. The low-magnification image in Fig. 4a reveals several network-like cracks as well as several spalling pits, which match well with the spalling failures shown in Fig. 3. A small area on the left-hand side was observed at a

Table 2
The mechanical properties of the manganese steel turnout.

HV_{30} (GPa)	Young Modulus (GPa)	UTS (MPa)	YS (MPa)	Elongation (%)	Area Reduction (%)	V-Notch Charpy energy (J)
1.9 ± 0.04	202 ± 6	773 ± 9	358 ± 9	47 ± 1	35 ± 4	197 ± 9

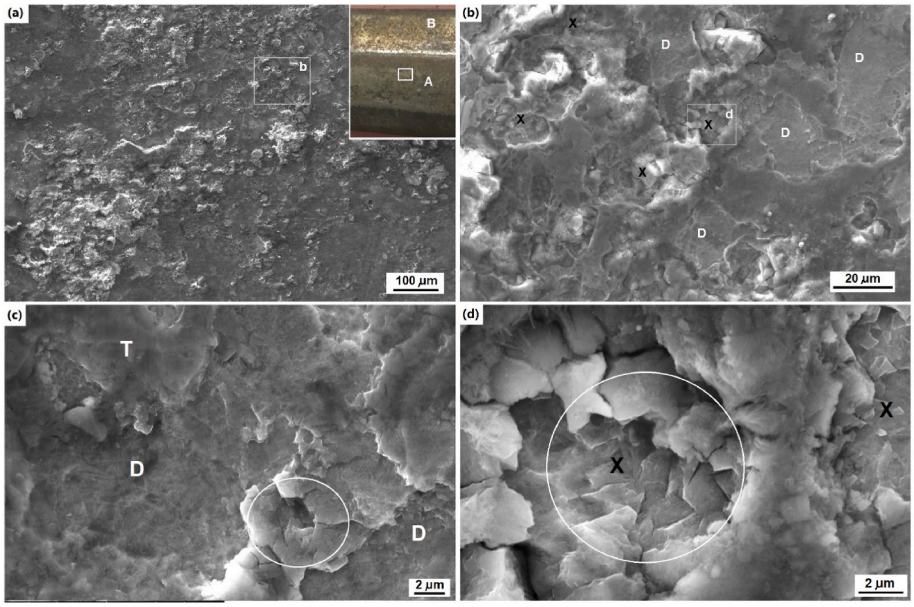

Fig. 3. SE image of the rail surface in the middle length (approximately 30 mm thick): (a) A low-magnification overview with an inserted photograph showing the observed area. (b) a medium-magnification image showing the morphology of a few deep spalling pits and areas of delamination. (c–d) High-magnification views of the highlighted areas in (b), showing fragments and brittle spalling.

higher magnification and is shown in Fig. 4b, which shows details of the cracks and spalling pits. In addition, the steel had been severely deformed, as being evidenced by the high-density deformation bands. A high-resolution observation of a small, highlighted area in the upper part of Fig. 4b is shown in Fig. 4c to show the fine structure of the deformation bands. In Fig. 4c, the middle area shows twins in two directions perpendicular to each other. These multi-twins have divided the matrix into micro-and sub-micro-scale cells. In addition, several bands exhibit high-density twins, e.g. 30 twinning lines having an average spacing of 233 nm, as labelled in the image. These findings confirm the occurrence of severe plastic deformation and are consistent to those published in literature regarding the deformation induced twins in austenitic manganese steel [4,6,16,34–37].

Extensive XRD characterisation determined that there was severe lattice distortion as a result of the deformation. The results are illustrated in Fig. 5 and Table 3. Fig. 5 compares the XRD curves acquired from the rail surface (see the insert in Fig. 3a for the location of XRD acquisition), the subsurface (approximately 0.1 mm beneath) and the bulk steel. The three curves all show diffraction peaks of the austenite phase. A major finding is the significant broadening of the peaks acquired from the rail surface, followed by less significant broadening of the peaks acquired from the subsurface region. Quantitative comparisons of the peak broadening are listed in Table 3. Both the rail top surface and the subsurface exhibit pronounced peak broadening and, correspondingly, high scales of microstrain and grain refinement. The microhardness values of the rail top and subsurface are $HV_{0.1}$ 8.7 GPa and $HV_{0.1}$ 5.2 GPa, respectively, which are substantially higher than the bulk hardness of $HV_{0.1}$ 2.4 GPa. The results demonstrate that the rail surface had been highly deformed and hardened. In addition, the (111) diffraction peak of the rail top exhibits extraordinary broadening to the right-hand side, which implies a small ferrite (110) diffraction peak. However, the (110) diffraction peak was not detected in the diffraction curves of the subsurface and bulk steel.

To confirm this important finding, repeated XRD scans were made at several places of the rail top. The presence of ferritic (110) diffraction is shown more clearly in the inserted Gaussian-fitting analysis in Fig. 5. The (110) peak was position at a diffraction angle (2θ) of 52.3°, revealing a d-spacing 0.2030 nm, which matches to the ferritic (110) lattice plane. It exhibits a peak breadth of 1.53° with a microstrain of 1.29% and a coherent scattering domain size of 6.4 nm, respectively. In literature, strain induced martensitic transformation was claimed as one of major hardening mechanisms of austenitic manganese steels. This mechanism was experimentally confirmed in several manganese steels, such as in medium-carbon and medium-manganese steels [8,9], and in low-carbon manganese steels [38]. However, such strain-induced martensite was not experimentally evidenced in Hadfield steels [4–6, 20,35]. To the best of our knowledge, this is the first time XRD characterisation has detected the ferritic phase in highly strained Hadfield steel, although further comprehensive characterisation is still expected. Moreover, the obtained austenitic (111) and (200) peaks exhibit irregular shapes, not fitting to a single Gaussian diffraction of homogeneous polycrystalline structure. By applying multiple Gaussian peak-fitting, each diffraction peak was found to match well to three sub-peaks with different FWHM values. The complex diffraction characteristic was derived from the heterogeneous substructure of the severely deformed austenite, which corresponds well to the heterogeneous distributions of nano-twins and deformation bands, as revealed by SEM observations, seeing Fig. 4.

Fig. 6 and Table 4 provide the results of XRD residual stress measurements. The plots between $(d\psi+d\text{-}\psi)/2$ and $\sin^2\psi$ exhibit good linear relationship whereas those between d and $\sin^2\psi$ show pronounced splitting. The splitting was mostly attributed to the complex strain-stress conditions, especially the existence of shear stresses. Nevertheless, both sides showed substantially high compressive stresses, namely, −648 ± 41 MPa and −504 ± 35 MPa for Side A and Side B respectively. The results are consistent to the severe straining and hardening as shown in

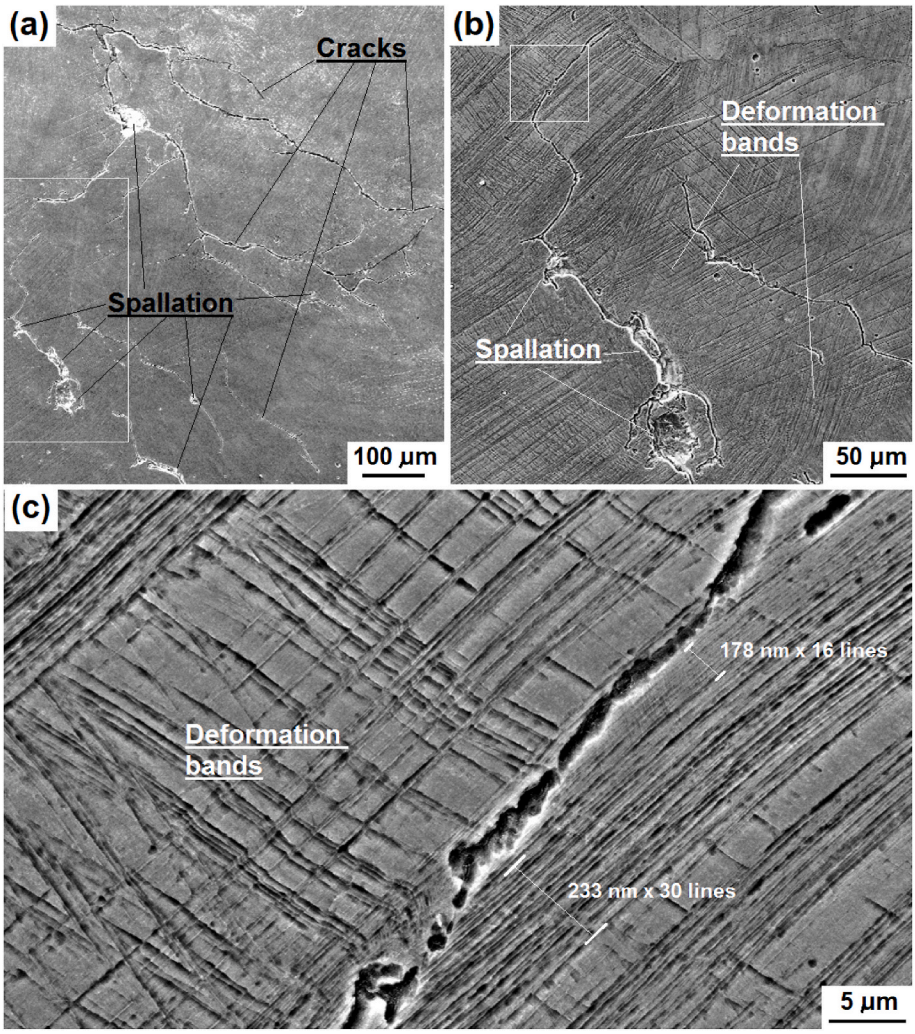

Fig. 4. SE images showing the microstructure of the turnout rail surface at depth of 20–40 μm: (a) A low-magnification view of the cracks and spallation. (b) A medium-magnification view of the deformation bands, cracks and spallation. (c) A high-magnification view of the high-density deformation twins besides an open crack, noticing the nano-twins inside each deformation band.

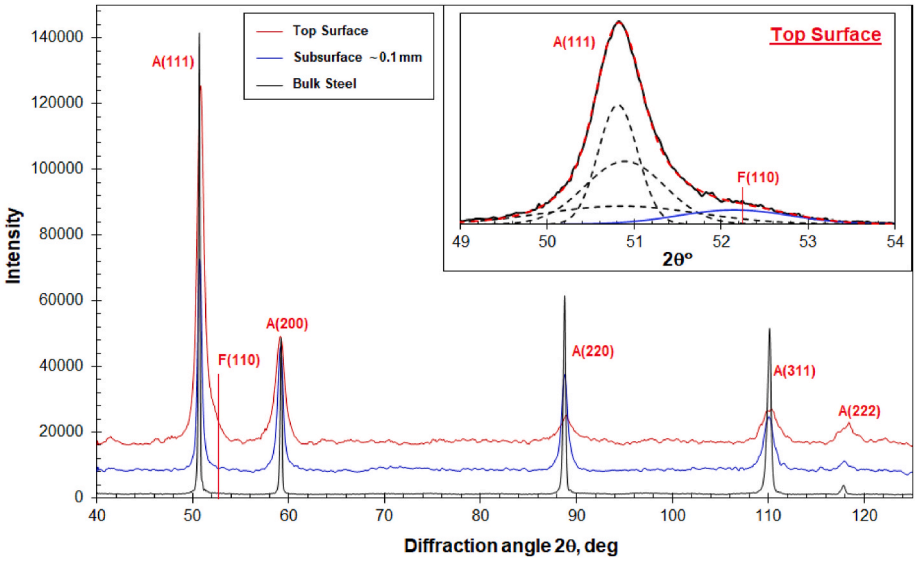

Fig. 5. XRD overall scans of top, subsurface and bulk.

Table 3
Comparison between the peak broadening, microstrain and coherent domain size of different places.

	FWHM (°)	Strain (%)	Domain size (nm)	$HV_{0.1}$ (GPa)
Rail Top	1.33 ± 0.55	0.64 ± 0.0.07	12 ± 3	8.7 ± 1.2
subsurface	0.77 ± 0.39	0.34 ± 0.05	22 ± 8	5.2 ± 0.3
Bulk	0.28 ± 0.07	0.10 ± 0.04	72 ± 15	2.4 ± 0.2

Figs. 4–6 and Table 3. In addition, comparison between the two methods shows that, the newly developed $(d_{\perp}\psi+d\text{-}\psi)/2 \sim sin^2\psi$ method provides comparable residual stress values to the traditional $d \sim sin^2\psi$ method. However, a significant advantage of the new method is the greatly reduced deviation, which is in good consistence to the previously reported measurements in other materials [31].

3.3. Cross-sectional characterisations of the rail subsurface

Transverse sections were prepared to characterise the microstructure and hardness property. Fig. 7a shows an optical microscopic image of the top part of one of the cross-sections, showing cracks and associated spalling formation. Fine cracks developed approximately 5 mm from the top surface, some of which are labelled by red arrows. Most cracks are either parallel to the top surface or at an incline angle. Obviously, the propagation of these cracks would eventually lead to a spalling block or a delamination sheet. The cross-sectional observations supplemented the top-views of spalling failure in Figs. 2 and 3. These subsurface cracking and spalling failures are comparable to those reported by other researchers [6,22,23]. Fig. 7b is an enlarged view of the top region of Fig. 3a, showing details of several major cracks within a depth of about 1 mm as well as several fine cracks in further depth. Meanwhile, the dense parallel lines in most grains are deformation bands which evidence the occurrence of severe plastic deformation. Fig. 7c shows similar deformation bands at a depth range of 1.8–3.1 mm, although at decreased severity. Several cracks have been formed in the upper part of the imaged area. Fig. 7d is an image taken at a depth of 3.8–5.0 mm, where the density of deformation had greatly decreased.

Optical microscopic observations revealed dense distribution of deformation bands in the subsurface areas where cracks and spalling failure had taken place. In the adjacent spalling-free and less cracked areas, however, the number of deformation bands was relatively less, which suggests different straining severity. To verify the different straining behaviour, microhardness measurements were made to compare the hardness depth profiles, shown in Fig. 8. Extremely high hardness values over $HV_{0.1}$ 6.9 GPa were measured in the spalling area at 10–20 μm deep, which was consistent with the hardness in the top rail of $HV_{0.1}$ 8.9 GPa. From approximately 1 mm the hardness stabilised at above $HV_{0.1}$ 5.9 GPa. These profiles are comparable to those hardness profiles of Hadfield steel turnouts reported in literature, whereas

Table 4
Residual normal stresses measured on the rail top zones.

Method	Side A	Side B
$d \sim \sin^2\psi$	−651 ± 355 MPa	−521 ± 304 MPa
$(d_{\perp}\psi+d\text{-}\psi)/2 \sim \sin^2\psi$	−648 ± 41 MPa	−504 ± 35 MPa

ultrahigh values beyond HV 6.9 GPa were rarely reported [20,22,39]. The extensive strain-hardening was associated with the occurrence of spalling failure. In contrast, the surface hardening in the spalling-free area was inferior, exhibiting maximum hardness of $HV_{0.1}$ 5.9 GPa at the depth of 10 μm and significantly reduced values below $HV_{0.1}$ 4.9 GPa in deeper positions. The overall strain-hardened depth was approximately 2 mm. In brief, the comparative microhardness testing indicates that, spalling failures occurred preferentially in the highly strain-hardened areas.

Figs. 9 and 10 show the details of cross-sectional SEM observations of the rail top on Side A. Fig. 9a is a low-magnification view showing a cross-section from the top edge. A major crack had developed from the rail surface to a depth over 0.2 mm, whereas the front edge of the crack propagation is shown in Fig. 10. Fig. 9b shows high-density deformation twins developed in close vicinity of the rail top, where observations at higher magnification indicated spacings of the twins to be 180–280 nm. Several fine cracks had developed beneath the top surface, which provide evidence of delamination wear. In addition, several short cracks orientated perpendicular to the twins were also visible. Fig. 9c shows twins in two orientations indicating multiple twinning deformation in the areas besides the major crack. Fig. 10 is a record of high-magnification observations of the propagation front of the major crack, of the area labelled '3' in Fig. 9a. The crack propagation can be seen to follow the orientation of the high-density nanotwins, seeing Fig. 10b and c.

Fig. 11 shows further subsurface cracking and microstructure evolution beneath the severely loaded Side A of the rail top. The location was inside the depth of serious spalling failure. When observed at several different magnifications, this zone was found to contain major cracks leading to spalling, fine cracks both parallel and perpendicular to the deformation bands, and high-density twins inside the deformation bands having inter-twin spacings of approximately 40–100 nm.

Fig. 12 presents the results of cross-sectional observations on Side B of the rail top. The observed area showed high-density deformation bands beneath a straight top edge, Fig. 12a. The deformation bands are in two orientations, in which the mechanical twins show spacings of 70–130 nm. Within approximately 3–5 μm from the top surface, following nital etching, a featureless microstructure was observed, indicating highly refined grain sizes. Moreover, the top edge was found to be free from delamination cracking, which agrees well with the results of visual inspection and residual stress measurements, confirming that Side B was less severely loaded than Side A. Nevertheless, severe plastic

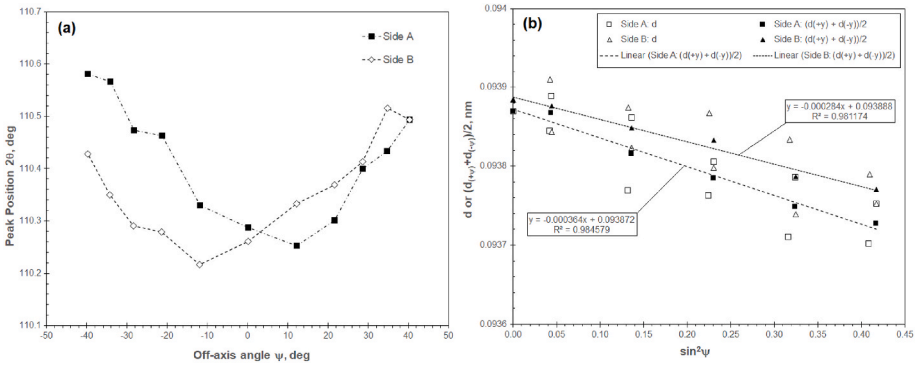

Fig. 6. XRD residual stress measurements on the two sides of the rail top: (a) The measured diffraction angles plotted versus the off-axis angles; (b) Plotting of d-spacing parameters (d and (dψ+d-ψ)/2) versus $\sin^2\psi$.

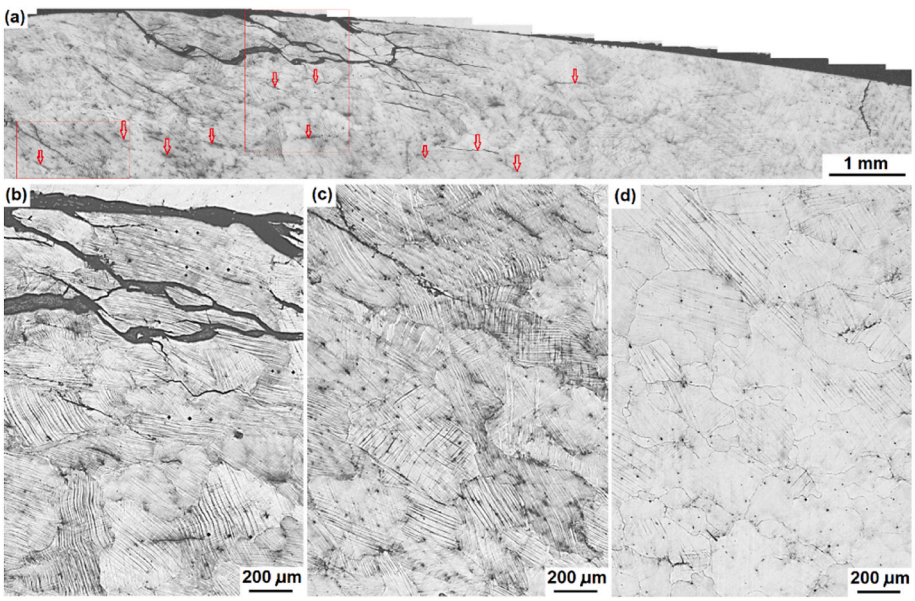

Fig. 7. Cross-sectional OPM of a spalling area. (a) Overall cross-sectional OPM; (b), (c) and (d) at depths of 0–0.6 mm, 1.8–3.1 mm and 3.8–5.0 mm, respectively, from the top surface.

deformation was confirmed in both sides.

3.4. Dry sliding properties of the rail top and the bulk steel

To evaluate the effect of strain hardening of the rail top on the wear resistance, comparative sliding wear tests were conducted on both the pre-ground and polished rail top, and the bulk steel. The results are shown in Figs. 13and14 and Table 5. Fig. 13 compares the friction behaviour of the samples under the 3-kg sliding tests. A high initial friction coefficient of approximately 0.4 was measured on the bulk Hadfield steel, which quickly increased to 0.6–0.7 within the first 10 min. After this initial running in period the friction coefficient dropped to below 0.4, before gradually increasing with increased sliding time, stabilising at 0.52–0.55. The friction coefficient of the rail top showed less variation stabilising at a high level close to 0.6 for the whole testing period.

Fig. 14 shows line profiles across the obtained wear tracks. At the applied three loads, the rail top sample exhibited significantly faster wear than the bulk steel. Moreover, it can be seen from the profiles that the wear tracks of the bulk steel all recorded pronounced plastic deformation of the steel resulting in the formation of material pile-up, above the normal surface, on the boundaries of the wear track. However similar pile-up was not observed in the wear tracks of the rail top, suggesting that little plastic deformation had occurred.

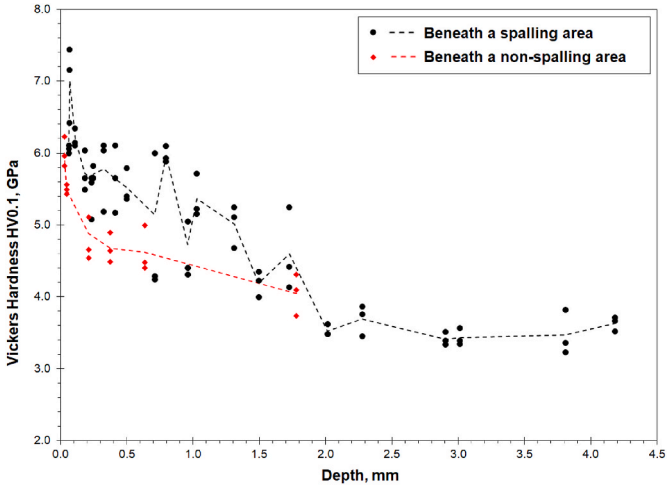

Fig. 8. Microhardness profiles beneath the rail top, measured in the subsurface area imaged in Fig. 7a.

Table 5 summarises the wear and friction coefficients and provides related interpretation. The average friction coefficient remained in a range between 0.50 and 0.60 regardless of the different load and surface hardening condition. However, the wear coefficient showed strong dependence on both the applied load and the sample condition. Firstly, the rail top showed higher wear coefficient than the bulk steel in all the applied loads. Secondly, the bulk steel exhibited a transition to fast wear when the applied load was increased from 3 kg to 5 kg, seeing the increase of relative wear (vs load) from 1.0, 1.6 to 7.8. A similar transition was also observed in the relative wear of the rail top, seeing the increase of relative wear from 1.0, 20.2 and 18.5. Obviously the transition to fast wear took place at the applied load of 3 kg, lower than the wear transition load of the bulk steel. In other words, the pre-hardened rail top is more sensitive to high-stress sliding wear than the bulk steel. The results suggest that substantial strain-hardening did not contribute to the wear resistance of the Hadfield steel. Instead, the wear resistance at heavy loading conditions became much worse.

4. Discussion

The results reported in this paper have revealed extensively the spalling failure of a Hadfield steel turnout, including the delamination and spalling observed on the rail top (Fig. 3) and the coalescence of subsurface cracks observed in cross-section (Fig. 7). The presence of subsurface cracks in close vicinity of the rail top surface caused the generation of delamination flakes, Figs. 7b, 9b and 11a, which formed mostly parallel to the rail surface. Meanwhile, those cracks exhibiting an inclined angle to the top surface had undergone propagation to certain depth, leading to large pieces of spallation, Fig. 7b–c and 9a. In brief, the microscopic observations confirmed delamination and spalling as the major failure of the Hadfield steel turnout, which is consistent to the onsite investigations, as shown in Fig. 1, and to the view of many other researchers [1,5–7,16,22–24].

It was found following experimental investigations that the delamination and spalling failures were associated with a gradient hardness

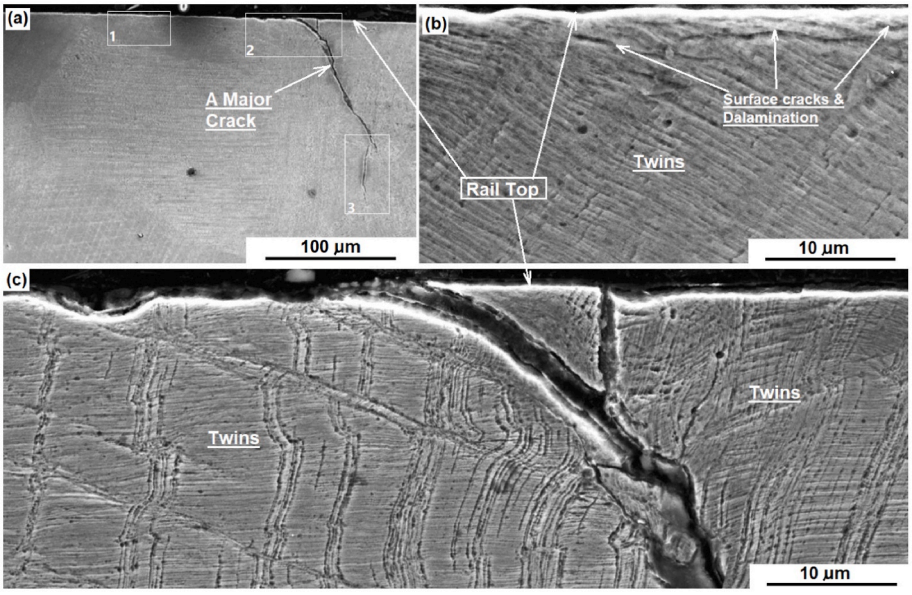

Fig. 9. SEM images showing cross-sectional views of Side A of the rail top: (a) A low-magnification overview; (b) High-magnification view of area '1' of the top edge; and (c) High-magnification view of area '2' of the top edge.

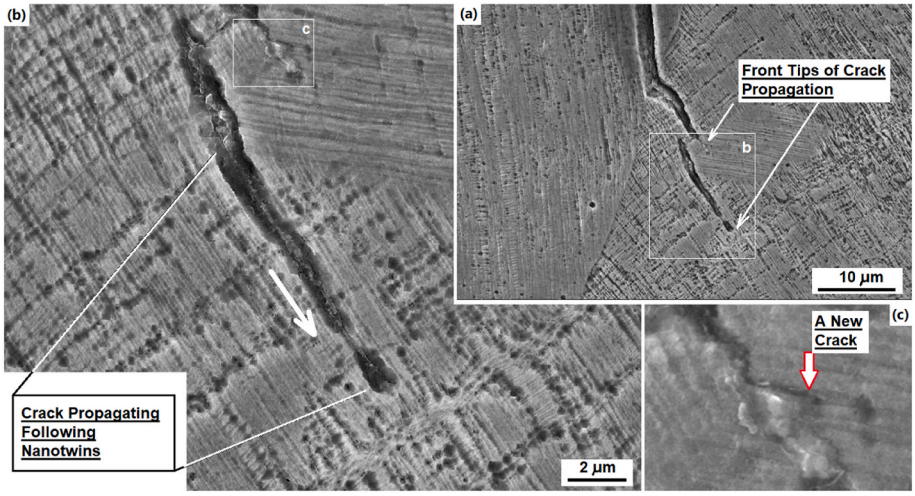

Fig. 10. Cross-sectional SEM images showing high-magnification views of the crack propagation edge: (a) Overview of the crack propagation edge; (b) The crack tip under propagation following the nano-twins; (c) Another crack tip following the direction of nanotwins.

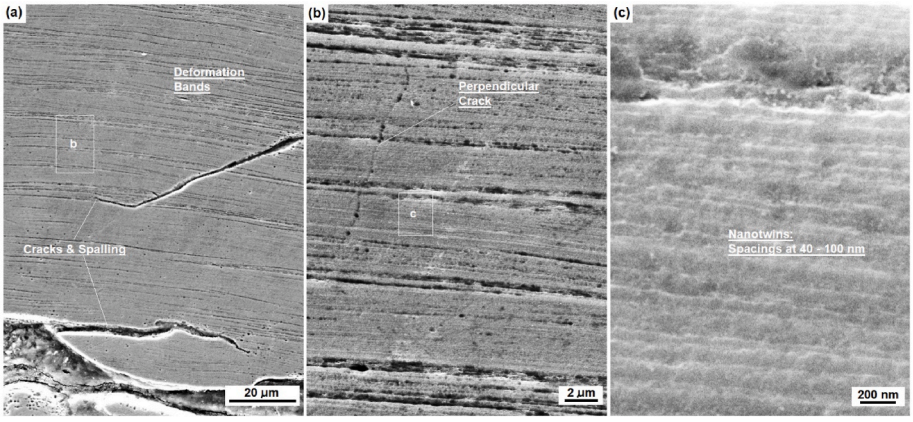

Fig. 11. Cross-sectional SEM images showing nanotwins in the severely deformed and cracked zone about 0.05–0.1 mm beneath the rail top: (a) The location of the observed area is within the depth of spalling failure; (b) A vertical crack had been generated in the severely deformed zone; (c) The high-density nanotwins.

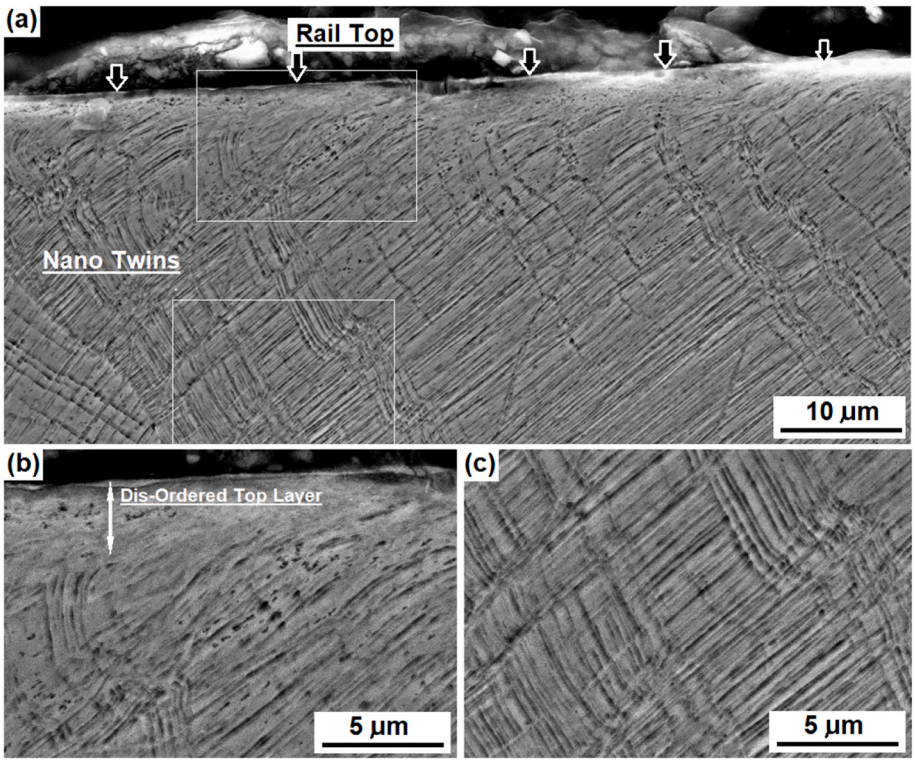

Fig. 12. Cross-sectional SEM images showing subsurface deformation in Side B of the rail top: (a) Overall view of the high-density deformation bands and the delamination-free top surface edge; (b) Details of the rail top edge; (c) Details of the nanotwins in two orientations.

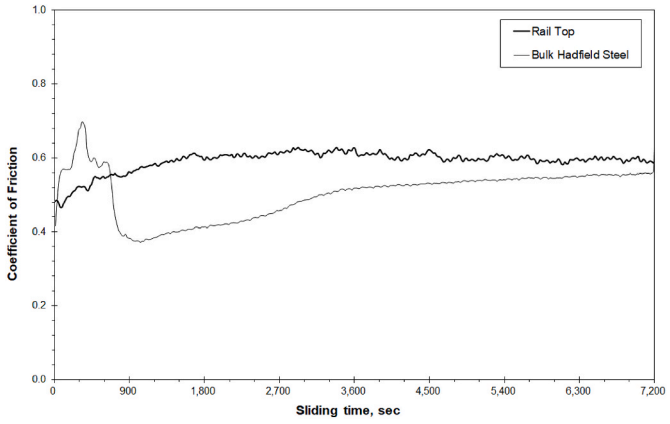

Fig. 13. Friction curves of the rail top and bulk steel samples.

profile with increased hardness above, the bulk steel, being observed from the top surface up to a depth of several millimetres, Fig. 8. While extremely severe hardening of the top rail resulted in a hardness of $HV_{0.1}$ 8.7 GPa, as shown in Table 3, it has been experimentally found that such extreme hardening triggered the brittle nature observed in the spalling areas. The brittle nature has been confirmed by the surface spalling failure (Fig. 3) and subsurface cracking as observed in plane-view (Fig. 4) and in cross-sectional view (Fig. 7 a-b, 9 b-c). Meanwhile, the subsurface hardness, in areas free from spalling cracks, was substantially lower than the cracked area, Fig. 8. In other words, subsurface cracking took place mostly in the severely hardened regions, where the hardness exceeded $HV_{0.1}$ 5.9 GPa. These hardness values were substantially higher than those reported on other wear conditions indicating that the severe deformation of the rail top resulted in strain hardening [22,25,29].

Along with the measured high hardness, the rail top layer was also found to have developed a significant residual compressive stress of 648 MPa. The scale of residual stress was far beyond the yielding stress of the bulk Hadfield steel, Table 2, which provides further evidence of the extreme strain hardening. It was reported that the yielding strength of Hadfield steel could be enhanced to a scale of 670 MPa when explosion hardening was applied resulting in an increased hardness to HB 330–350 [24]. The explosion hardening, however, was also found to greatly decrease the impact toughness property from approximately 190 J/cm^2 of the austenitic bulk steel to less than 60 J/cm^2 of the hardened steel. Nevertheless, these experimental findings suggested the correlation between the extreme hardening and the embrittlement. The combined extreme scale of hardening, embrittlement and residual compressive stress are believed to be responsible for the occurrence of delamination and spalling.

The strain induced hardening and embrittlement can be explained by the microstructural characteristics determined by the experiments. It has been documented that the strain hardening mechanisms of austenitic manganese steels include mechanical twinning, dynamic strain aging, multiplication of dislocations, and interactions of slipping dislocations with various slipping barriers such as twins, stacking faults, Mn-C covalent bonded clusters, and dislocation walls and cells [12–14,16,17,19]. The current XRD characterisation has revealed significant peak broadening of austenite, Fig. 5 and Table 3, which can be considered as an evidence of increased lattice distortion and decreased sizes of elastic scattering domains, although the latter was termed as grain refining [40]. The current XRD characterisation has also revealed heterogeneity of the strained substructures by resolving each diffraction peak as sub-peaks of different broadening widths, Fig. 5. The heterogeneity has been partly demonstrated by the heterogeneous distribution of mechanical twins as revealed in SEM observations, Figs. 4, 9 and 12. These XRD and SEM characterisations of highly strained austenitic matrix are consistent with the literature [6,7,16,35,41,42]. Despite these, an important new finding of current research was that the resultant twins not only enhanced the strain hardening, but also provided a channel for subsurface crack propagation, Figs. 10 and 11. This implies a

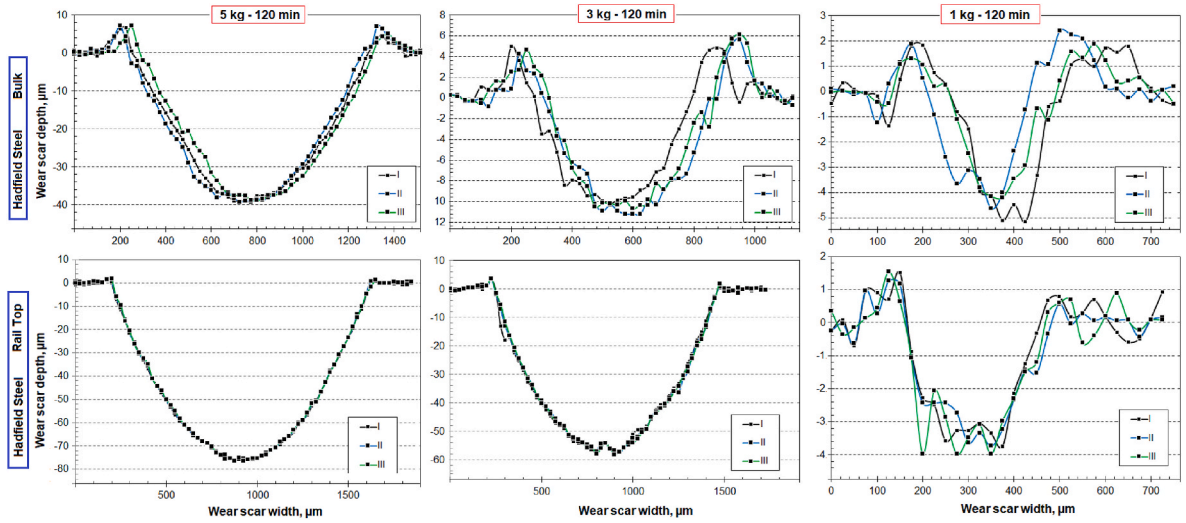

Fig. 14. Wear measurements of the rail top and bulk steel samples.

Table 5
The wear and friction properties of rail top ($HV_{0.1}$ 5.2 GPa) and bulk steel ($HV_{0.1}$ 2.7 GPa).

Properties	Samples	Applied load		
		1 kg	3 kg	5 kg
Friction Coeff.	**Bulk**	0.58 ± 0.06	0.50 ± 0.07	0.52 ± 0.07
	Rail Top	0.57 ± 0.10	0.59 ± 0.03	0.59 ± 0.02
Wear Coeff. (10^{-15} $m^3N^{-1}m^{-1}$)	**Bulk**	11.8 ± 1.3	19.5 ± 2.7	92.7 ± 1.6
	Rail Top	14.0 ± 0.7	283.2 ± 0.1	258.9 ± 1.2
Relative Wear	**Bulk**	1.0	1.6	7.8
	Rail Top	1.0	20.2	18.5

contribution of the mechanical twins to the strain induced embrittlement and helps explain the significantly increased wear in the hardened rail top, when compared to the bulk steel, Figs. 13–14 and Table 5.

Another new finding of this paper is the confirmed diffraction peak derived from highly strained ferritic phase, Fig. 5, which evidenced the presence of tetragonal martensite in the rail top. This finding would be able to clarify the doubt about the occurrence of strain-induced martensite transformation in high-carbon and high-manganese austenitic Hadfield stee [6,13,18,29]. Obviously, further high-resolution electron microscopy is necessary to resolve the structural morphology of such a martensitic structure. Nevertheless, the (110) diffraction of martensite was only detected on the outmost rail top. Such strain induced martensite has not been observed in the high-carbon and high-manganese Hadfield steel, however it was reported in several austenitic manganese steels, such as in low-carbon high-manganese TRIP steels and in medium-manganese steels [8,9,44,45]. In contrast, the disappearance of such (110) in other highly strained subsurface depth agreed well to most published works that severe deformation of Hadfield steels did not induce martensitic transformation [19,40]. In those papers, TEM observations repeatedly showed nanotwins and high-density dislocations with complex substructures. In this paper, the extremely broad peaks of martensite and austenite of the rail top suggest greatly decreased sizes of the elastic scattering domains, which can be assumed to be comparable to those TEM observed nanocrystalline structures of worn surfaces [24,40,41,45–47].

The comparative sliding wear tests performed in current research indicate that, strain hardening of Hadfield steel made it suffer from substantially faster wear than the bulk steel. Unlike the bulk steel which exhibited pile-ups besides the wear scars as an evidence of plastic deformation during the wear tests, the pre-strain-hardened rail top showed no pile-up but significantly increased wear scar depth. This behaviour was consistent with the recently published work on the sliding wear mechanisms of Hadfield steel that the values induced strain hardening made the worn surface more brittle and consequently triggered brittle spalling wear [29]. In literature, shot peening treatments of Hadfield steels were reported to lead to surface hardening and structural nanocrystallisation [40,43]. Whereas the resultant hardening promised lower wear for limited peening time, over peening was found to cause remarkably worse wear resistance because of peening induced surface cracking [40]. These results help explain the contribution of strain hardening to the embrittlement, delamination and spalling failures of Hadfield steel.

In summary, the current research has demonstrated that, the Hadfield steel turnout failed predominantly by delamination and spalling as a result of severe surface deformation. The deformation led to an extreme scale of strain hardening and embrittlement as evidenced by the high hardness and the subsurface cracking. The extreme straining of the rail top brought about highly disordered austenitic substructure as well as marginal but evident transformation to martensite. The strain induced nanotwins were detrimental to the wear resistance.

5. Conclusions

A turnout of austenitic Hadfield steel has been found to exhibit brittle delamination and spalling failure on its rail top surface. Through comprehensive experimental investigation, the failure has been confirmed to be resulted from the following reasons:

1) A gradient hardness profile has been determined indicating severe strain-induced hardening and embrittlement. Subsurface cracking took place in the regions being hardened to $HV_{0.1}$ 5.9 GPa or higher, whereas the subsurface regions free from cracks showed hardness lower than $HV_{0.1}$ 4.9 GPa.
2) The strain-induced embrittlement has been demonstrated in the accelerated wear in comparative sliding wear tests between the rail top and the bulk Hadfield steel.
3) The progressive accumulation of plastic deformation led to dense deformation bands in the coarse austenite grains at a depth of up to 2 mm beneath the rail top. These deformation bands comprised of densely packed mechanical nanotwins, which have been found to facilitate crack propagation.

4) Strain induced tetragonal martensite was detected by quantitative XRD analysis of the rail top in addition to the highly deformed austenite, which co-existed with extraordinary surface hardness of $HV_{0.1}$ 6.9–8.9 GPa.
5) An extremely high residual compressive stress of 500–650 MPa has been measured on the rail top surface.

Declaration of competing interest

The authors declare that they have no known competing financial interests or personal relationships that could have appeared to influence the work reported in this paper.

References

[1] S.G. Wang, Current status and future development trend of railway turnouts in China, Railw. Eng. 10 (2015) 42–46.
[2] M. Wiest, W. Daves, F.D. Fischer, H. Ossberger, Deformation and damage of a crossing nose due to wheel passages, Wear 265 (2008) 1431–1438.
[3] S.L. Issomura, S.M. Pessanha, C.V.C. Rocha, L.A.S. Lopes, L.A.C.M. Aragaso Filho, Turnout frogs evaluation under heavy haul railway traffic, Int. J. Civil & Environmental Engineering IJCEE-IJENS 16 (2016) 1–8.
[4] S.L. Guo, D.Y. Sun, F.C. Zhang, X.Y. Feng, L.H. Qian, Damage of a Hadfield steel crossing due to wheel rolling impact passages, Wear 305 (2013) 267–273.
[5] Y.N. Dastur, W.C. Leslie, Mechanism of work-hardening in Hadfield manganese steel, Metall. Trans. A 12 (1981) 749–759.
[6] O.A. Zambrano, G. Tressia, R.M. Souza, Failure analysis of a crossing rail made of Hadfield steel after severe plastic deformation induced by wheel-rail interaction, Eng. Fail. Anal. 115 (No) (2020), 104621.
[7] C. Efstathiou, H. Sehitoglu, Strain hardening and heterogeneous deformation during twinning in Hadfield steel, Acta Mater. 58 (2010) 1479–1488.
[8] Z.M. He, Q.C. Jiang, S.B. Fu, J.P. Xie, Improved work-hardening ability and wear resistance of austenitic manganese steel under non-severe impact-loading conditions, Wear 120 (1987) 305–319.
[9] F. Zhang, T. Lei, A study of friction-induced martensitic transformation for austenitic manganese steel, Wear 212 (1997) 195–198.
[10] Z. Li, Y. Wang, X. Cheng, Z. Li, C. Guo, S. Li, The effect of rolling and subsequent aging on microstructures and tensile properties of a Fe-Mn-Al-C austenitic steel, Mater. Sci. Eng. A822 (2021). No. 141683.
[11] Y. Feng, R. Song, Y. Wang, M. Liu, H. Li, X. Liu, Aging hardening and precipitation behaviour of Fe-31.6Mn-808Al-1.38C austenitic cast steel, Vacuum 181 (No) (2020), 109662.
[12] J.P. Xie, W.Y. Wang, J.W. Li, A.Q. Wang, Y.R. Zhao, L.L. Li, Wear Resistant Austenitic Manganese Steels, Science Press, Beijing, 2008.
[13] J. Zhao, P. Zhang, Self-strengthening mechanism of high- and middle manganese steel hardfacing layer, China Surf Eng 19 (2006) 28–32.
[14] F. Gauzzi, M. Rossi, B. Verdini, Cold-working induced martensitic transformation in 12 percent Mn austenitic steel (Hadfield steel), Metall. Italiana 63 (1971) 555.
[15] G. Tweedale, W.D.M. Paton, Sir robert abbott Hadfield F.R.S (1858-1940) and the discovery of manganese steel, notes and records, The Royal Society Journal of The History of Science 40 (1985) 63.
[16] C. Chen, B. Lv, H. Ma, D. Sun, F. Zhang, Wear behaviour and the corresponding work hardening characteristics of Hadfield steel, Tribol. Int. 121 (2018) 389–399.
[17] B. Hutchinson, N. Ridley, On dislocation accumulation and work hardening in Hadfield steel, Scripta Mater. 55 (2006) 299–302.
[18] Y. Xu, Y. Chen, J. Xiong, J. Zhu, Mechanism of strain-induced nanocrystallization of Hadfield steel under high energy impact load, Acta Metall. Sin. 37 (2001) 165–170.
[19] C. Cai, R. Song, S. Liu, Y. Feng, Z. Pei, Wear behaviour and subsurface layer work hardening mechanism of Fe-24.1Mn-1.21C-0.48Si steel, Procedia Eng. 207 (2017) 2251–2256.
[20] S. Kahrobaee, E.Z. Karimi, Characterisation of work-hardening in Hadfield steel using non-destructive eddy current method, Nondestr. Test. Eval. 34 (2019) 178–192.
[21] S.G. Peng, R.B. Song, T. Sun, Z.Z. Pei, C.H. Cai, Y.F. Feng, Z.D. Tan, Wear behaviour and hardening mechanism of novel lightweight Fe-25.1Mn-6.6Al-1.3C steel under impact abrasion conditions, Trbo Lett 64 (2016). No. 13.
[22] H.M. Guo, W.J. Wang, T.F. Liu, J.H. Liu, J. Guo, Q.Y. Liu, Analysis of damage behaviour of heavy-haul railway rails, China Mech. Eng. 25 (2014) 267–272.
[23] O.A. Zambrano, Y. Aguilar, J. Valdes, S.A. Rodriguez, J.J. Coronado, Effect of normal load on abrasive wear resistance and wear micromechanisms in FeMnAlC alloy and other austenitic steels, Wear 348–349 (2016) 61–68.
[24] F. Zhang, B. Lv, C. Zheng, M. Zhang, S. Yang, Z. Yan, Failure mechanism and worn surface microstructure of high manganese steel and bainite steel crossings, Chin. J. Mech. Eng. 44 (2008) 232–238.
[25] S. Dhar, M.K. Danielsen, R. Xu, Y. Zhang, F.B. Grumsen, C. Rasmussen, D.J. Jensen, Residual strain-stress in manganese steel railway crossing determined by synchrotron and laboratory X-rays, Mater. Sci. Technol. 37 (2021) 6–13.
[26] B.D. Cullity, S.R. Stock, Elements of X-Ray Diffraction, third ed., Pearson Education Ltd, 2014, p. 379, 402.
[27] E.A. Badawi, M.A. Abdel-Rahman, A. Mostafa, M. Abdel-Rahman, Determination of the crystallite size and micro-strain by novel method from XRD profile, Appl. Phys. 2 (2019) 1–15.
[28] Q. Luo, Characterization of short-range ordered domains using quantitative X-ray diffraction, Nanosci. Nanotechnol. Lett. 10 (2018) 835–842.
[29] Q. Luo, J. Zhu, Wear property and wear mechanisms of high-manganese austenitic Hadfield steel in dry reciprocal sliding, Lubricants 10 (2022). No. 37.
[30] I.C. Noyan, J.B. Cohen, Residual Stress Measurement by Diffraction and Interpretation, Springer-Verlag, New York, 1987.
[31] Q. Luo, A modified X-ray diffraction method to measure residual normal and shear stresses of machined surfaces, Int. J. Adv. Manuf. Technol. 119 (2022) 3595–3606.
[32] V.G. Navas, O. Gonzalo, I. Quintana, T. Pirling, Residual stresses and structural changes generated at different steps of the manufacturing of gears: effect of banded structures, Mater. Sci. Eng. 528A (2011) 5146–5157.
[33] S. Eck, H. Oßberger, U. Oßberger, S. Marsoner, R. Ebner, Comparison of the fatigue and impact facture behaviour of tive different steel grades used in the frog of a turnout, Pro. IMechE Part F: J Rail and Rapid Transit 228 (2014) 603–610.
[34] P.C. Machado, J.I. Pereira, A. Sinatora, Subsurface microstructural dynamic recrystallization in multiscale abrasive wear, Wear 486–487 (2021), 204111.
[35] F. Zhang, C. Chen, B. Lv, H. Ma, E. Farabi, H. Beladi, Effect of pre-deformation mode on the microstructures and mechanical properties of Hadfield steel, Mater. Sci. Eng. A743 (2019) 251–258.
[36] L.B. Varela, G. Tressia, M. Masoumi, E.M. Bortoleto, G. Regattieri, A. Sinatora, Roller crushers in iron mining, how does the degradation of Hadfield steel components occur? Eng. Fail. Anal. 122 (2021), 105295.
[37] M. Weiss, K. Mester, A. Taylor, N. Stanford, A critical assessment of deformation twinning and epsilon martensite formation in austenitic alloys during complex forming operations, Mater. Char. 145 (2018) 423–434.
[38] I. Nikulin, T. Sawaguchi, K. Ogawa, K. Tsuzaki, Effect of γ to ε martensitic transformation on low-cycle fatigue behaviour and fatigue microstructure of Fe-15Mn-10Cr-8Ni-xSi austenitic alloys, Acta Mater. 105 (2016) 207–218.
[39] R. Harzallah, A. Mouftiez, E. Felder, S. Harriri, J.P. Maujean, Rolling contact fatigue of Hadfield steel X120Mn12, Wear 269 (2010) 647–654.
[40] W. Yan, L. Fang, Z. Zhang, K. Sun, Y. Xu, Effect of surface nanocrystallization on abrasive wear properties in Hadfield steel, Tribol. Int. 42 (2009) 634–641.
[41] Y. Lv, S. Li, F. Chen, R. Zhu, T. Lei, On the impact abrasive wear of super-high manganese steel, Acta Metall. Sin. 35 (1999) 581–584.
[42] C. Chen, B. Lv, X. Feng, F. Zhang, H. Beladi, Strain hardening and nanocrystallisation behaviours in Hadfield steel subjected to surface severe plastic deformation, Mater. Sci. Eng. A729 (2018) 178–184.
[43] Y. Xu, Y.M. Chen, J.L. Xiong, J.H. Zhu, Mechanism of strain-induced nanocrystallization of Hadfield steel under high energy impact load, Acta Metall. Sin. 37 (2001) 165–170.
[44] L. Wang, P. Yang, W. Mao, Analysis of martensitic transformation during tension of high manganese TRIP steel at high strain rates, Acta Metall. Sin. 52 (2016) 1045–1052.
[45] L. Wang, P. Yang, K. Li, F. Cui, W. Mao, Phase transformation and texture evolution during cold rolling and α'-M reversion in high manganese TRIP steel, Acta Metall. Sin. 54 (2018) 1756–1766.
[46] Q. Luo, H.J. Mei, M. Kitchen, Y. Gao, L. Bowen, Effect of short-term low-temperature austempering on the microstructure and abrasive wear of medium-carbon low-alloy steel, Met. Mater. Int. 27 (2021) 3115–3131.
[47] Q. Luo, J. Li, Q. Yan, W. Li, Y. Gao, M. Kitchen, L. Bowen, N. Farmilo, Y. Ding, Sliding wear of medium-carbon bainitic/martensitic/austenitic steel treated by short-term low-temperature austempering, Wear 476 (2021), 203732.